Unravelling Heterodyne Force Microscopy

Verbiest, G.J.

CHAPTER 2

Ultrasonic Rayleigh Scattering by Subsurface Nanoparticles

Recent experiments in the field of Subsurface Atomic Force Microscopy demonstrate that it is possible to nondestructively image micro- and even nanoparticles that are embedded deeply within the bulk of a significantly softer sample. In order to get insight into the contrast formation mechanism, we performed a finite element analysis and an analytical study, in which we calculate the amplitude and phase variation on the surface of an ultrasonic wave that has travelled through the sample. Our calculations are performed as closely as possible to the situation in the experiments to enable a (future) comparison based on our predictions. We show that Rayleigh scattering of acoustic waves accounts for the measured contrast and we verify the characteristic Rayleigh dependencies. The numerical results show that the contrast is independent of the depth at which a particle is buried, whereas the analytical study reveals a 1/depth dependence. In addition, we find a large deviation in the width of the particle in the contrast at the surface when applying the numerical or the analytical calculation, respectively. These results indicate the importance of both the reflections of sound waves at the sample interfaces and bulk damping, as both are treated differently in our two models.

Most of this chapter is published in [28]

2.1 Introduction

For many fields and applications it has always been a desire to image beneath the surface of a sample, especially in a nondestructive way. However, it also has always been a challenge in microscopy to obtain subsurface information. The ongoing progress in many research areas, such as nanotechnology, material science, thin film technology, medical science, biology, and the semiconductor industry, increases the desire to obtain subsurface information in a nondestructive way, while simultaneously pushing the demands on the resolution even further, as one wishes to image buried micro- and even nanostructures.

By combining ultrasound technology with Atomic Force Microscopy, Kolosov and Yamanaka invented Ultrasonic Force Microscopy [4] and later Yamanaka and Nakano introduced the waveguide Ultrasonic Force Microscopy [5]. In an Ultrasonic Force Microscope (UFM) an ultrasonic wave is launched from the bottom of the sample and picked up by the AFM-tip at the sample surface and in a waveguide-UFM the sound wave is directly launched through the AFM-cantilever (tip). An UFM gives access to some subsurface information, whereas the waveguide-UFM provides mainly access to the elasticity in the near surface region. In 2000 the Kolosov group tried to obtain quantitative subsurface information by combining the UFM and the waveguide-UFM and thereby inventing the Heterodyne Force Microscope (HFM) [2, 3]. Making use of the nonlinear tip-sample interaction, this technique relies on the frequency mixing of the ultrasonic wave that travels trough the sample with an ultrasonic wave at a different frequency that is launched via the AFM-cantilever. By tuning the nonlinear difference frequency to a (higher) eigenmode of the cantilever, the signal amplitude is amplified [13]. From the nonlinear difference frequency that can be measured with the AFM, one can extract the amplitude and the phase of the usually not directly accessible ultrasonic wave that travelled through the sample. As buried objects or voids alter the propagation of the sound wave, both the amplitude and the phase must contain quantitative information on subsurface features. Alternatively, the subsurface scatterer induces variations in the local elastic response of the sample [29,30], which can lead to variations in the nonlinear tip-sample interaction, and thus in the amplitude and phase of the difference frequency.

Although several experiments have been performed with this technique [3, 6, 8–12, 14, 31], a quantitative understanding of the contrast mechanism, which depends on the wave propagation in the samples in combination with the tip-sample interaction, is still missing. Recent studies investigate the working principle of this technique [3, 32, 33]. Cuberes [3] points out the increased phase sensitivity in the difference frequency due to the mixing, and Cantrell and Cantrell [32] show that the phase of the sound wave that travelled through

the sample measured on the surface corresponds one-to-one with the phase of the nonlinear difference frequency. This tells us that the phase at the sample surface is measured more accurately on the lower difference frequency than on the original, higher ultrasonic frequency [34, 35]. A recent paper by Tetard et al. [33] addresses the generation of the nonlinear difference frequency by the tip-sample interaction. They show that the amplitude is maximal in the region where the *Van-der-Waals* interaction is dominant.

Pushing the resolution, Shekhawat and Dravid reported in 2005 on the detection of gold nanoparticles with a diameter of only $\sim$ 17.5 nm embedded 500 nm deep in a polymer (poly(2-vinylpyridine)) [6]. In the same paper they also report on the detection of voids in copper interconnect lines. Although they simply used Heterodyne Force Microscopy, they called their technique Scanning Near-Field Ultrasound Holography. To prevent further confusion, we would like to officially introduce Subsurface-AFM [14], referring to all ultrasonic AFM techniques that give access to quantitative information on objects below a surface. In 2007 Cantrell and Lillehei [8] published that it is even possible to detect gold nanoparticles with a diameter of $\sim$ 12.5 nm embedded 7 μm deep in the polymide LaRC$^{\text{TM}}$-CP2.

In order to enable a quantitative understanding and to gather new insight in the physics of the detection mechanism, a theory is urgently needed that predicts the amplitude and the phase on the sample surface of an ultrasonic wave that has travelled through a sample with embedded nanoparticles. We studied the acoustic wave propagation in a polymer containing spherical gold particles of different sizes and at different depths using both an analytical calculation and a finite element analysis (FEA). To enable a comparison with reported experiments [6, 8, 9], we calculate our results for ultrasonic waves of a few Megahertz (MHz) and nanoparticles with a radius between 10 and 100 nm.

This chapter is organized as follows. Firstly, we present some general remarks, definitions and boundary conditions used in our calculations. Then we explain the analytical and the FEA model, respectively, including their validities. Using both models, we verify the usual Rayleigh dependencies and predict the amplitude and the phase of the sound wave that travelled through the sample evaluated at the sample surface. The next part addresses the depth dependence and the lateral resolution. We compare our results with experiments reported in literature, before we end with the main conclusions.

2.2 General Considerations and Definitions

In Subsurface-AFM, the typical frequency of the wave that travels through the sample, is in the order of a few MHz. The size of subsurface particles and voids observed in experiments range typically between 20 and 350 nm and the thicknesses of the used samples are between 0.1 and 25 μm. For

sound speeds between 2350 m/s for a polymer, like polymethyl methacrylate (PMMA), and 3900 m/s for copper, the longitudinal wavelength of a MHz sound wave ranges between 2.4 and 3.9 mm, which is not only more than 10000 times larger than the size of the biggest defects studied (200 nm) but also more than 5000 times larger than the used sample thicknesses (500 nm). Based on these length scales one expects Rayleigh scattering for sound waves, with the following dependencies of the (complex) amplitude, A_s, of the scattered wave:

$$A_s \propto f^2, \quad A_s \propto \Delta\rho/\rho, \text{ and } \quad A_s \propto R^3 \tag{2.1}$$

where f stands for frequency, $\Delta\rho/\rho$ for the relative density difference between the particle and the medium, and R for the particle's radius[1].

Figure 2.1 shows a cross section of the geometry to be calculated, in which we also define the variables that we will use in the rest of this chapter. Table 2.1 provides an overview on the material properties that we used in the calculations. In addition, we define $\Delta\rho$ as the density difference between the nanoparticle and the bulk and ΔK as the difference in bulk moduli. We use $\Delta\rho$ and ΔK to study the dependence on the material properties.

In order to define an amplitude contrast, C_A, and a phase contrast, C_ϕ, we need a reference value of the (complex) amplitude $A(\vec{r_1})$ at the surface for a sample without embedded scatterer. As this amplitude is equivalent to the amplitude on the surface far away from the scatterer, $A(|\vec{r_1}| \to \infty)$, we define

$$C_A(\vec{r_1}) = \frac{|A(\vec{r_1})| - |A(|\vec{r_1}| \to \infty)|}{|A(|\vec{r_1}| \to \infty)|} \tag{2.2}$$

$$C_\phi(\vec{r_1}) = \phi(\vec{r_1}) - \phi(|\vec{r_1}| \to \infty) \tag{2.3}$$

The effect of scattering on the contrasts is largest directly above the scatterer. Therefore we usually calculate C_A and C_ϕ for $\vec{r_0}$. An exception is the evaluation of the contrasts on the surface as a function of the distance away from the scatterer; here we explicitly calculate $C_\phi(|\vec{r_1} - \vec{r_0}|)$.

In both the analytical calculation and the finite element analysis we have to deal with sample boundaries, at which, in general, sound waves are partly reflected, but also partly transmitted into the surrounding medium. It will turn out that the amount of reflection and transmission plays an important role in the formation of the contrasts. In the analytical calculation we used the acoustic impedance mismatches at the interfaces to calculate the amount of reflection and transmission at the boundaries for the incoming wave from the bottom of the sample. As this approach is impossible for the scattered sound waves in the applied model, the boundaries in the analytical calculation are treated fully transparent for the scattered waves. In other words, the scattered sound waves are completely transmitted into the surrounding medium. In

[1] Note that the scattered intensity is given by the $|A_s|^2$.

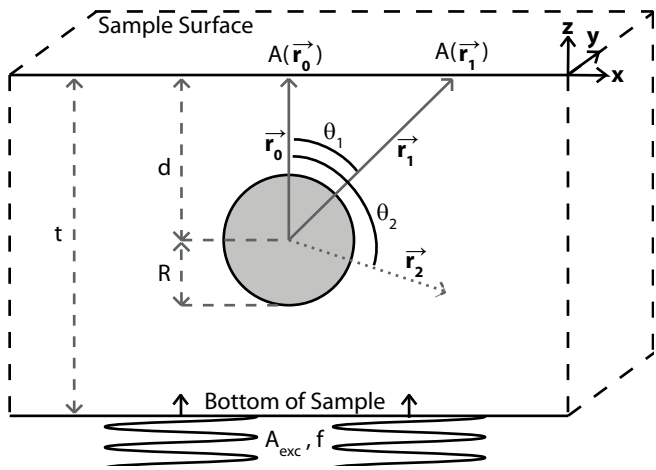

Figure 2.1: Cross section of the geometry to be calculated. We define the following variables. $|\vec{r_0}|$: minimal distance from the center of the nanoparticle (in gray) to the sample surface; $|\vec{r_1}|$: distance from the nanoparticle to a position somewhere on the sample surface; $|\vec{r_2}|$: distance from the nanoparticle to a position somewhere in the sample; θ_i: angle between $\vec{r_0}$ and $\vec{r_i}$ (i = 1,2); R: radius of the nanoparticle; d: depth of the nanoparticle; t: sample thickness; and A_{ext}, f: amplitude and frequency of the excitation. Note also the definition of our Cartesian coordinate system.

Property Units	ρ kg/m^3	E GPa	K GPa	G GPa	v_L m/s	L_α(3 MHz) m
Au	19700	78	220	27	3240	5.3
PMMA	1200	2.4	5.91	2.25	2350	0.033

Table 2.1: The material properties used in the models: ρ is the density, E is the Young's modulus, K is the bulk modulus, G is the shear modulus, v_L is the longitudinal sound velocity, and L_α is the attenuation length.

the finite element analysis we used fully reflective conditions for all boundaries, as it is technically very difficult to take into account also the effect of acoustical impedances. We attribute the significant different results of the analytical calculations and FEA to the differences in the treatment of the boundary conditions.

2.3 Analytical Calculation

In order to derive an analytical model that also accounts for reflections on both the top and the bottom of the sample (see Fig. 2.1), we first calculate an effective incident wave from the interference of all reflected waves of the original excitation at the top and bottom interface taking into account damping in the sample material in the form of the attenuation length (L_α). This results in an unscattered wave with a frequency dependent amplitude A_{eff} (see Appx. 2.A). Using this effective incident wave at the position of the particle as an input, we then calculate the scattered waves for all positions on the sample surface by applying scattering theory in the Rayleigh limit [36,37]. Finally, the addition of the effective incident wave and the scattered waves (at the sample surface) describes the interference pattern at the sample surface: $A(\vec{r_1}) = A_{eff} + A_s(\vec{r_1})$. It is important to notice that we introduce two approximations with this approach. Firstly, as the theory for the scattered waves is valid only for an infinitively large sample, we neglect all reflections of the scattered waves at the sample interfaces. Secondly, the effective amplitude, A_{eff}, will be smaller in the close vicinity above the particle, due to the energy loss that is transferred into the scattered wave. However, we expect this loss to be negligible, as the scattering cross section [2] for a sound wave of 3 MHz at a gold spherical nanoparticle with a radius of 50 nm embedded in PMMA is in the order of 10^{-54} m^2.

To implement the scattering of sound, we need an analytical theory that is valid at the desired length scales. Although phonon scattering in the Rayleigh limit at atomically sized features has been described analytically [38], the use of simple, classical continuum theory of elasticity is fully justified in our case, as the considered particle and void sizes are larger than 20 nm, which significantly exceeds the interatomic distance. Using the equation of motion in an isotropically elastic solid medium, the scattering at a spherical particle (or void) in an infinitely large sample has been solved analytically [36, 37]. Both derivations reflect the typical Rayleigh dependencies of Eq. 2.1: the cross section for scattering on a spherical object with different mass and elasticity than the surrounding material scales with f^4 and R^6. Following Ying and Truell [36], we write the scattered fields for the longitudinal and shear mode waves outside the spherical nanoparticle as:

$$\Psi_s(\vec{r_2}) = \sum_{m=0}^{\infty} A_m h_m(k_1|\vec{r_2}|) P_m(cos(\theta_2)) \tag{2.4}$$

$$\Pi_s(\vec{r_2}) = \sum_{m=0}^{\infty} B_m h_m(\kappa_1|\vec{r_2}|) P_m(cos(\theta_2)) \tag{2.5}$$

[2] The scattering cross section is the scattered intensity divided by the incoming intensity, which is proportional to A_s^2/A_{eff}^2.

where A_m and B_m are the amplitude of the m^{th} longitudinal and shear wave mode respectively, $h_m(x)$ is the spherical Hankel function of the first kind, and $P_m(x)$ is the Legendre polynomial of degree m. $\vec{r_2}$ and θ_2 are defined as in Fig. 2.1. k_1 and κ_1 are the wave numbers in the bulk corresponding to the longitudinal and shear wave velocity, respectively: $k_1 = 2\pi f/\sqrt{\frac{K+\frac{4}{3}G}{\rho}}$ and $\kappa_1 = 2\pi f/\sqrt{\frac{G}{\rho}}$. G, K, and ρ are given in Tab. 2.1.

In order to account for attenuation (damping) for both the scattered waves and effective incident wave, we treat the wave numbers complex by adding an imaginary part that equals $1/L_\alpha$.

In the following we evaluate the analytical description on the Rayleigh dependencies of Eq. 2.1. It is shown in [36] that, in the Rayleigh limit, the expansion coefficients A_0, A_1 and A_2 (and corresponding B_0, B_1 and B_2) scale in the same way as the square root of the scattering cross section, and that all higher order coefficients, $m > 2$, can be neglected in Eqs. 2.4 and 2.5, as k_1R and κ_1R are much smaller than 1 and all terms with $m > 2$ scale with $(k_1R)^{2m-1}$ or $(\kappa_1R)^{2m-1}$. Please note that we took order coefficients up to m = 10 into account when calculating the amplitude and phase contrasts shown in the graphs of Sect. 2.5. When evaluating the coefficients up to $m = 2$ on the dependencies of the radius R, the wave number k_1, and the density difference $\Delta\rho$, we find:

$$A_0 \propto k_1^2R^3, \qquad B_0 = 0 \tag{2.6}$$

$$A_1, B_1 \propto i\frac{\Delta\rho}{\rho}k_1^2R^3 \tag{2.7}$$

$$A_2, B_2 \propto k_1^2R^3 \tag{2.8}$$

On the surface far away from the scatterer ($|\vec{r_1}| \to \infty$), we only have a contribution from the effective incident wave, A_{eff}. Right above the particle, at $\vec{r_0}$, we have the interference of the effective incident wave, A_{eff}, and the scattering wave, A_s, of which the main amplitude coefficients are provided in Eqs. 2.6, 2.7, and 2.8. Assuming a small scattering amplitude ($A_s << A_{eff}$), we can make a Taylor expansion of the expected contrasts (see Appx. 2.B):

$$C_A \propto \frac{Re(\overline{A_{eff}}A_s)}{|A_{eff}|^2} \tag{2.9}$$

$$C_\phi \propto \frac{Im(\overline{A_{eff}}A_s)}{|A_{eff}|^2} \tag{2.10}$$

Since the amplitude A_{eff} of the unscattered, effective incident wave is constant everywhere for a fixed frequency, both the amplitude and the phase contrast show the Rayleigh dependencies of the scattered amplitude, A_s, of which the coefficients are given in Eqs. 2.6, 2.7, and 2.8. This implies that

both contrasts at the surface scale with the volume of the particle and the density difference: R^3 and $\Delta\rho/\rho$, respectively, reflecting the standard Rayleigh dependencies of Eq. 2.1. The frequency dependence is not as obvious, as both the effective incident amplitude, A_{eff}, and the values of the Hankel function in Eqs. 2.4 and 2.5 do depend on the frequency in a non-trivial way.

However, if a frequency range exists where A_{eff} as well as the Hankel functions can be regarded constant, we expect to observe a f^2 behavior according to Eqs. 2.9 and 2.10. Therefore also the frequency dependence follows the standard Rayleigh dependence, but only for a certain frequency range.

Finally, we would like to summarize the important limitations of this analytical model explicitly, as these shortcomings are expected to explain any deviations with experimentally determined contrast values. Firstly, the top and bottom interfaces are treated fully transparent for the scattered waves. Reflections at these interfaces are considered only for the external, incoming wave leading to the effective incident wave. Finally, we also neglect the decrease in intensity of the effective incident wave caused by the scattering at the particle.

2.4 Finite Element Analysis (FEA)

In a second approach, we apply FEA to calculate the frequency response of a sample with an embedded particle to an ultrasonic excitation from the bottom of the sample (see Fig. 2.1). We used the commercially available *multi-physics package* of COMSOL [39] and chose the isotropic model that determines the displacement vector $\vec{s}$ for each isotropically elastic solid medium by solving the equation of motion for $\vec{s}$:

$$k_1^{-2}\nabla\nabla\cdot\vec{s}+\kappa_1^{-2}(\nabla^2\vec{s}-\nabla\nabla\cdot\vec{s})+\vec{s}=0 \tag{2.11}$$

The material parameters used, the Young's moduli (E), the shear moduli (G), the attenuation length (L_α), and the densities (ρ) are provided in Tab. 2.1. The forces on the system can be specified separately for each boundary. Plane acoustic waves are generated at the bottom interface by applying a small sinusoidal displacement perpendicular to this interface. This boundary condition leads to a full reflection of the incoming wave at a "fixed-end". The top surface of the sample is free to move, thereby following the acoustic oscillations that arrive there and leading to a full reflection at a "free-end". Using FEA we calculate the displacements of the sample for a specified frequency, (f), resulting in the amplitude and phase at each point in the sample from which we determine C_A and C_ϕ on the surface.

The FEA calculation requires the division of the sample into a finite number of small elements, which is called meshing. The limited number of meshing elements prevents us from modelling samples with realistic dimensions. It is

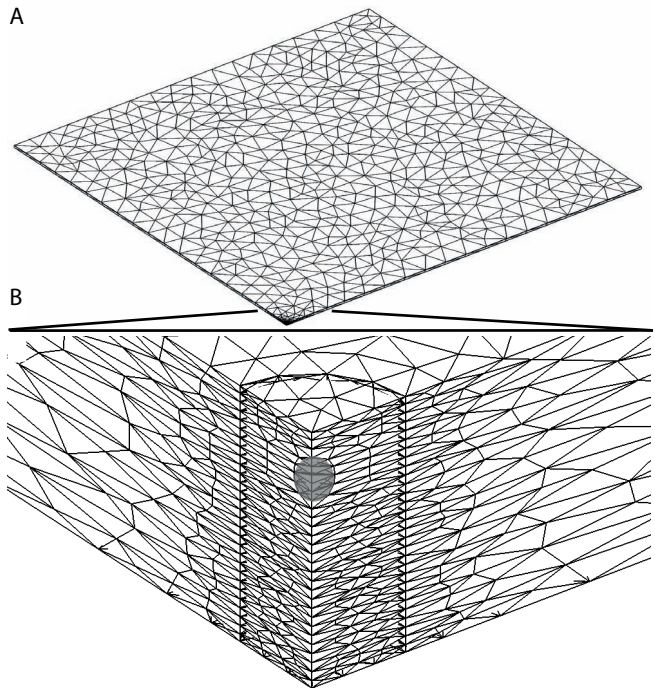

Figure 2.2: The mesh simulation box (A) with a magnification of the corner (B), in which the particle (indicated by the gray circle) is situated.

impossible to account for lateral (x, y) sample dimensions of several cm's and simultaneously retain sufficient resolution to calculate the scattering from inclusions smaller than 100 nm. The number of elements is reduced by using the internal symmetries of the sample, as we only need to calculate one quarter of the sample (see Fig. 2.2). A further reduction in the number of elements is achieved by changing the element size within the mesh according to the desired accuracy: the mesh is kept sufficiently fine close to the scatterer and gets much coarser further away from the particle (see Fig. 2.2). Still we also had to reduce the lateral sample size. This introduces another problem: scattered waves (with horizontal components) will repeatedly reflect at the sides of the sample (fully reflecting boundaries), especially as the attenuation length in PMMA at 3 MHz is as large as 3.3 cm [40].

These reflective boundary conditions effectively produce a lattice of scatterers with a lattice constant a, which is equal to the sample size and twice the simulation box size L_B ($a = 2L_B$). In order to investigate (and finally to remove) the artificially created lattice effect, we had to reduce the attenuation length. As it is possible to define different attenuation lengths along the differ-

ent directions in the FEA, we denote the attenuation length in the horizontal direction of the sample with $L_{\alpha,xy}$ and the attenuation length in the z-direction with $L_{\alpha,z}$.

In order to determine the minimal required horizontal sample size that suppresses interference effects arising from the reflections at the sample sides, we calculated C_ϕ as a function of simulation box size and attenuation length (see Fig. 2.3). L_B is varied from 500 nm to 0.1 mm and L_α is varied from realistic ($L_\alpha = 3.3$ cm) to 100× stronger attenuation. Different symbols indicate different attenuation lengths and the calculations were performed with $L_{\alpha,z} = L_{\alpha,xy}$ except for the most right points that lie within in the dotted black box. These data points were determined by applying a perfectly matched layer (PML) in the horizontal direction of the sample. A PML constantly increases the attenuation as a function of the distance from the scatterer such that sound waves are not reflected back from the edges of the sample. The PML covers the entire width of the sample except for a small cylindrical region around the scatterer. It turned out that, even with a PML, it is not possible to reduce the attenuation length below 0.014 cm, which has to be compared to $L_\alpha = 3.3$ cm.

Inspecting the phase contrast in Fig. 2.3, one notices that, initially, $C_\phi(\vec{r_0})$ increases linearly with L_B/L_α. When the width of the sample is large enough or the damping is sufficiently strong (at $L_B/L_\alpha \simeq 0.1$), reflections at the sample sides are suppressed and interference effects vanish. The remaining contrast is solely generated by a single scatterer in a very wide sample. A further increase of the sample size or damping is without any effect leading to a constant value of $C_\phi(\vec{r_0})$. This is verified also by the data points that refer to the application of a PML (dotted box in the graph).

This picture is confirmed by the phase contrasts on the sample surface that are calculated for different ratios of L_B/L_α and that are shown in Fig. 2.3B, 2.3C, and 2.3D. The absence of any interference effects in Fig. 2.3B is because the lateral sample size becomes comparable to the width of the scatterer: this results in a three layer system without significant scattering to the sides. Alternatively, one can describe this low ratio of L_B/L_α by considering a very small damping (large L_α). Scattered waves with a horizontal component bounce back and forth between the sample sides leading to a homogeneous background without interference and a decreased phase contrast directly above the scatterer. When increasing the simulation box size the data points start to deviate from the linear dependence, because interference effects occur in the sample (see Fig. 2.3C). Finally, at large box sizes or sufficiently large damping interference effects vanish, as can be seen in Fig. 2.3D.

We can explain the initial linear dependence of the phase contrast on L_B/L_α for small box sizes. The number of times a wave passes by at a (surface) location is in the order of $\frac{L_\alpha}{2L_B}$. As the sum of phases of the waves arriving at this location has to be divided by the number of waves, the total phase contrast

scales with $\left(\frac{L_\alpha}{2L_B}\right)^{-1} \propto \frac{L_B}{L_\alpha}$. The signal scales linearly with L_B/L_α up to the point where L_B becomes about one tenth of the size of L_α. On the basis of this result, we expect damping to play a critical role.

By choosing the largest possible horizontal sample size with proper attenuation length, we are able to approximate a sample of realistic dimensions while simultaneously ensuring that we simulate the scattering mechanism correctly. These simulations had approximately 15.000 mesh elements and took a few minutes on a decent desktop computer.

The FEA calculations in the rest of this chapter are performed with a horizontal simulation box size L_B of 0.1 mm and a thickness t = 500 nm. The radius of the scatterer R is 50 nm (except for Fig. 2.6); the depth of the scat-

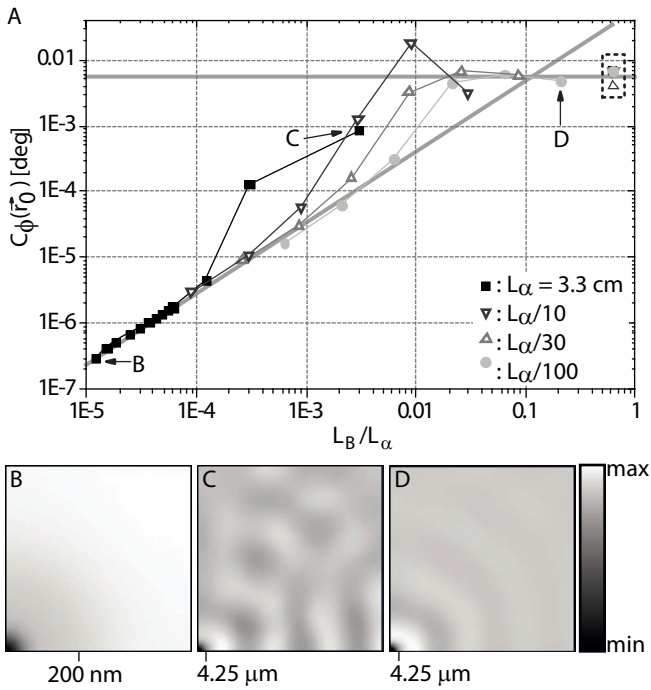

Figure 2.3: (A) The phase contrast as a function of L_B/L_α. The four curves represent different damping within the material: ■= realistic attenuation (L_α = 3.3 cm), $\bigtriangledown$ = 10× stronger, $\bigtriangleup$ = 30× stronger and • = 100× stronger. The data points located in the dotted black box are obtained with a perfectly matched layer (see text) and L_α = 0.014 cm. The grey lines are a guide to the eye. The figures (B), (C), and (D) show C_ϕ at the surface for different box sizes and attenuation lengths indicated with the arrows in (A). The half-width-half-max of the phase contrast is indicated with a tick below the figure.

terer is 200 nm (except for Fig. 2.6 and 2.7); the excitation frequency f is 3 MHz (except in Fig. 2.4); and we chose $\Delta\rho = \rho_{Au} - \rho_{PMMA}$ (except for Fig. 2.5). The attenuation lengths had to be chosen such that $L_{\alpha,xy} = 0.14$ mm and $L_{\alpha,z} = 0.33$ mm (100× stronger damping).

2.5 Results and Discussion

To investigate the Rayleigh dependencies we calculated the amplitude and phase contrast as a function of the excitation frequency, density difference and particle radius (see Fig. 2.4, 2.5 and 2.6).

Figure 2.4 shows $C_A(\vec{r_0})$ and $C_\phi(\vec{r_0})$ for both the analytic calculations and the FEA as a function of the excitation frequency. Only for the special case of $\Delta\rho = 0$, we observe a quadratic frequency dependence in the FEA results, which is characteristic for Rayleigh scattering, for frequencies ranging from 2 to 100 MHz. For the realistic case of $\Delta\rho = \rho_{Au} - \rho_{PMMA}$ the quadratic frequency dependence breaks down, which is in accordance with our expectations, as explained in Sect. 2.3. In addition, both $C_A(\vec{r_0})$ and $C_\phi(\vec{r_0})$ are up to 4 orders of magnitude larger than in the case of $\Delta\rho/\rho = 0$. Therefore, a main contribution to the contrast comes from the density difference between the scattering particle (or void) and the bulk of the sample.

Figure 2.5 shows $C_A(\vec{r_0})$ and $C_\phi(\vec{r_0})$ as a function of the density difference between the particle and bulk of the sample. Please note that $\Delta\rho$ starts at -1. $\Delta\rho = -1$ represents a void in PMMA. The linear dependence of the FEA results confirms the Rayleigh dependence and verifies our expectation. Please note that we varied the density of the particle and not the density of the bulk. The reason for this is that an increase in the bulk density would lead to a deviation from a linear dependence, as k_1 would change and thus the values of the Hankel functions as well as the effective incident wave A_{eff} (see Sect. 2.3). When comparing the FEA with the analytical results, one notices the different slopes. This is caused by the multiple reflections of the external incoming wave as well as the scattered wave A_s (in the direction of $\pm\vec{r_0}$) at the top and bottom interfaces of the sample. This process involves also multiple (higher order) scattering at the particle of both the external incoming wave as well as the scattered waves. As the boundary conditions for reflections are treated differently in the FEA and the analytical calculations, the contrast in the FEA will be higher or lower depending on the thickness of the sample. Realizing that the amount of reflections is independent of $\Delta\rho$, one expects a linear dependence of the contrast on $\Delta\rho$, but with different slopes for the different models.

Figure 2.6 shows $C_A(\vec{r_0})$ and $C_\phi(\vec{r_0})$ as a function of both the particle radius R and the particle depth d. The first thing one notices is that all curves obtained by FEA (solid lines) fall on top of each other in both the amplitude and the phase contrast. The FEA results show no depth dependence of the particle. This is in contrast to the analytical results (dashed lines), which

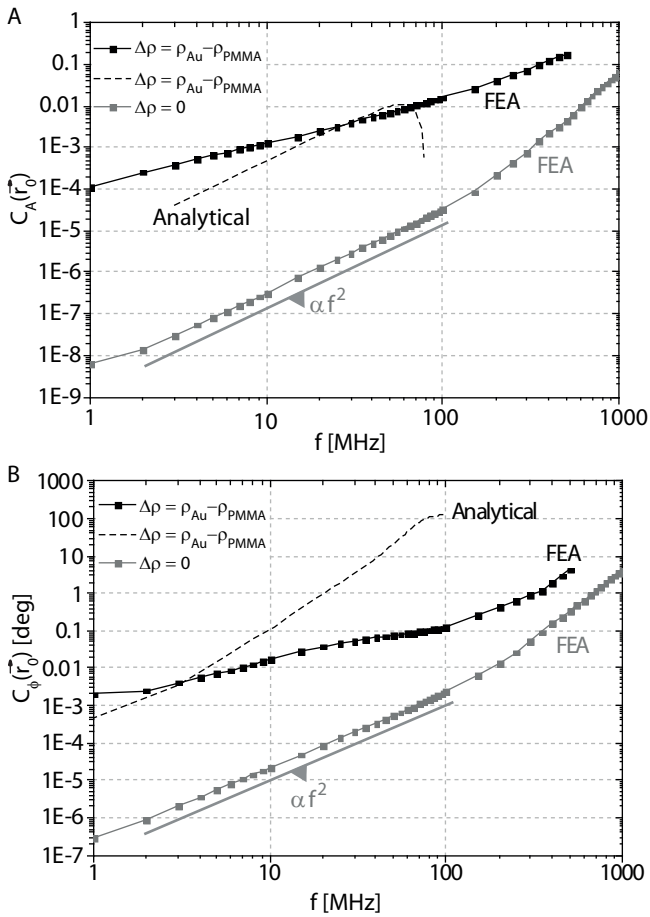

Figure 2.4: The amplitude contrast (A) and the phase contrast (B) calculated as a function of the excitation frequency. The plots in black show the case for a gold particle with radius R = 50 nm embedded d= 200 nm deep in PMMA taken into account $\Delta\rho = \rho_{Au} - \rho_{PMMA}$. The gray plots are calculated for the specific case of $\Delta\rho = 0$ to verify the Rayleigh dependence of f^2 for low frequencies.

show a $1/d$ dependence for both the amplitude and the phase contrast. This dependence can be understood when considering that, in general, the intensity of a scattered wave is distributed over a sphere with a radius that equals the distance to the scatterer. Therefore, the scattered intensity, $|A_s|^2$, decreases with d^2. As the amplitude and phase contrast for small scattering amplitudes are given by Eqs. 2.9 and 2.10 respectively, both contrasts are expected to be inversely proportional to the depth, which is indeed the case for the analytic

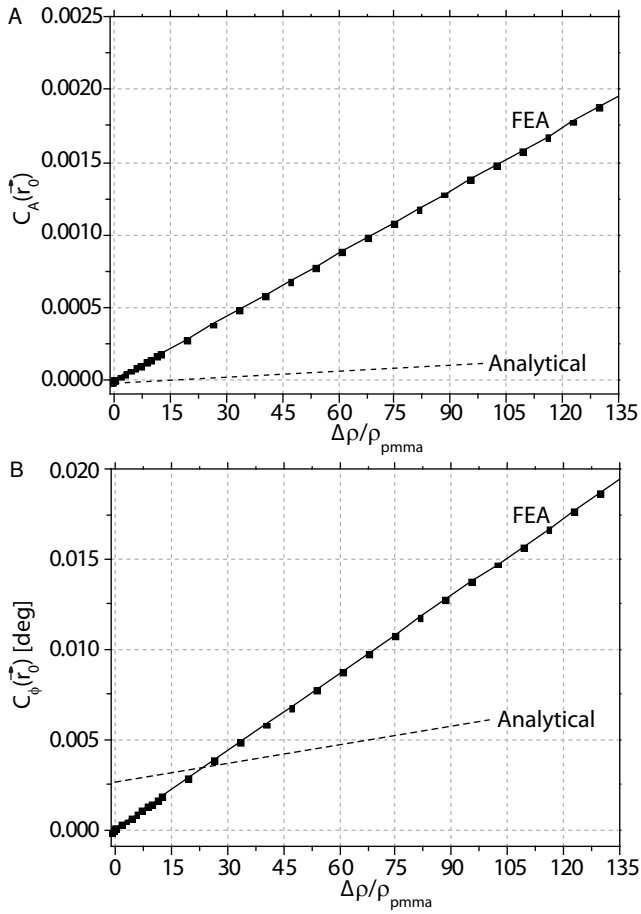

Figure 2.5: The amplitude contrast (A) and the phase contrast (B) calculated as a function of $\Delta\rho$. The plots are calculated for a particle with radius R = 50 nm embedded d= 200 nm deep in PMMA with $\Delta\rho = \rho_{Particle} - \rho_{PMMA}$ and excited with a frequency of f = 3 MHz. Please note that $\Delta\rho$ starts at -1. $\Delta\rho = -1$ represents a void in PMMA.

calculations.

The absence of a depth dependence in the FEA results is unexpected, and can only be explained by the different boundary conditions for reflections at the interfaces. The number of reflections in the FEA is enormous and can be estimated by the ratio $L_{\alpha,z}/t \approx 700$. These reflections diminish the depth dependence in the FEA calculations. More specifically, it can be shown that the depth dependence comes solely from the contribution of the scattered wave

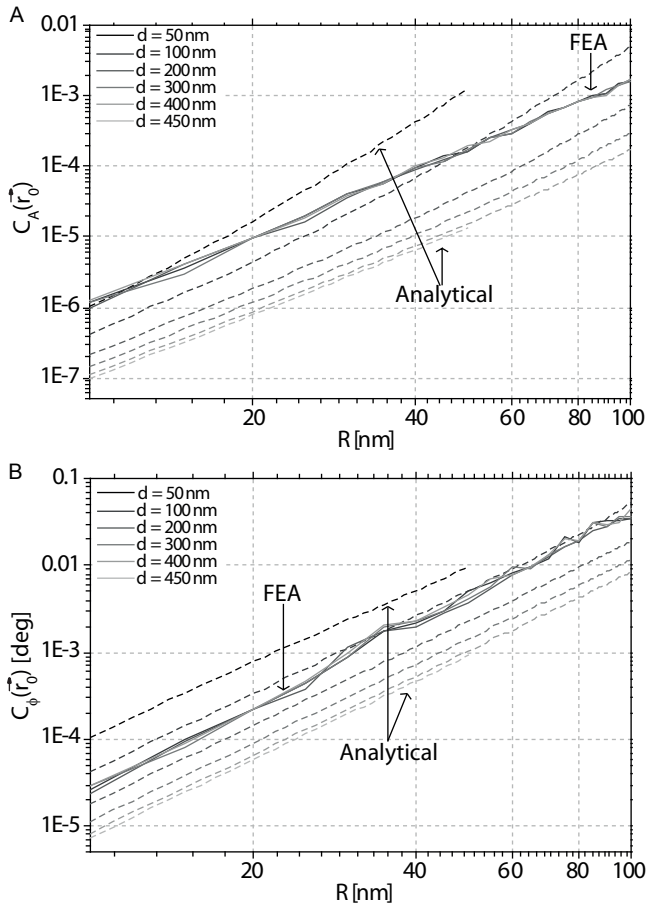

Figure 2.6: The amplitude contrast (A) and the phase contrast (B) calculated as a function of particle radius R and particle depth d. The depth d varies from 50 nm to 450 nm indicated by lines that vary from black to light gray. The FEA results, indicated with solid lines, show no depth dependence (all curves fall on top of each other), whereas the analytical results, indicated with dashed lines, do show a 1/d dependence. The plots show the case for a gold particle with radius R embedded d nm deep in PMMA with $\Delta\rho = \rho_{Au} - \rho_{PMMA}$ and excited with a frequency of f = 3 MHz.

(in the $\pm\vec{r_0}$ direction) and not from the remaining part of the external incoming wave (see Appx. 2.C). The multiple (higher order) scattering of the scattered wave(s) average out the depth dependence. As reflections of the scattered wave are totally neglected in the analytical calculations, we clearly observe a depth

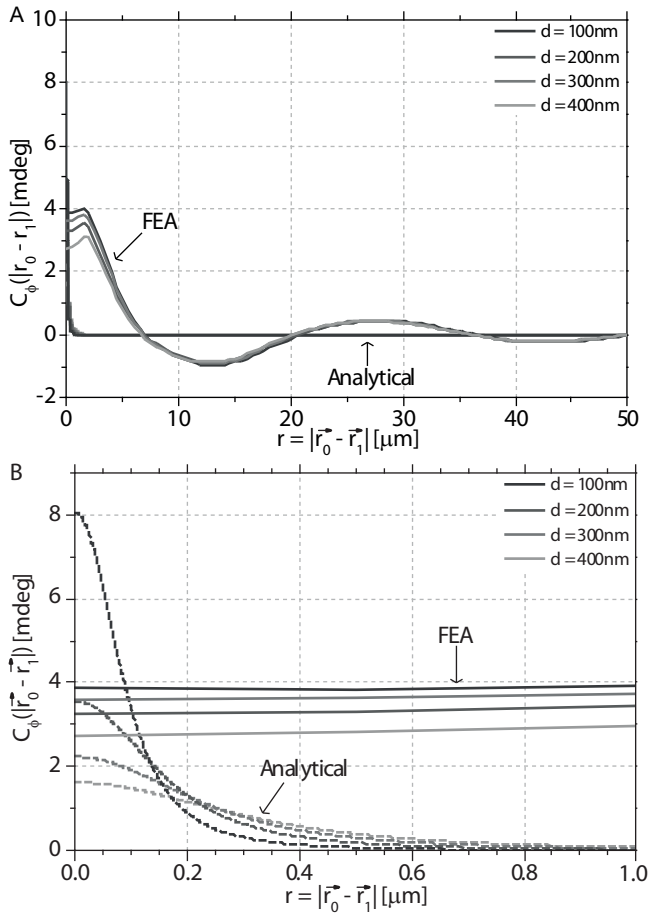

Figure 2.7: (A) and (B) show the phase contrast on the surface as a function of $r = |\vec{r_0} - \vec{r_1}|$ for different length scales. The plots are calculated for a gold particle with radius R = 50 nm embedded in PMMA with $\Delta\rho = \rho_{Au} - \rho_{PMMA}$ and excited with a frequency of f = 3 MHz. The depth d of the particle varies from 100 nm to 400 nm indicated by a gray scale that varies from black to light gray respectively. Notice the interference pattern in the FEA results for large r as well as the difference in the widths between the FEA and the analytical calculation at HWHM for r = 0.

dependence in these results.

This effect of multiple reflections is verified also in Fig. 2.7, which shows the phase contrast [2] on the surface calculated analytically and by FEA as a

[2] As the amplitude contrast shows smaller values that are more difficult to measure experimentally, we restrict these calculations to the phase contrast only.

function of $r = |\vec{r_0} - \vec{r_1}|$ and depth d. In the FEA results, the phase contrast right above the particle at $r = 0$, depends on the depth of the particle, but does so in a non-monotonic way. Please note that the curve at a depth of 300 nm shows a higher contrast than the curve at a depth of 200 nm. For larger distances r away from the particle, we see oscillations in the phase contrast: there is a minimum at ~ 13 μm, a maximum at ~ 27 μm, and another minimum at ~ 42 μm. We attribute this interference pattern to the multiple reflections at the upper and lower sample interface in the z-direction. In addition to the interference, we observe that if the width of the peak at $r = 0$ (right above the particle) is significantly different for the FEA calculations. The Half Width Half Maximum (HWHM) of the peak in the FEA result is approximately 4 μm, while the HWHM of the peak in the analytical results is between 100 and 400 nm. Both differences, the interference pattern and the HWHM, are again due to the multiple reflections in the FEA that are absent in the analytical calculation.

Considering soft (biological) materials and their much lower elasticities, the expansion coefficients in Eqs. 2.6, 2.7, and 2.8 are increased and we expect a larger amplitude and the phase contrast in comparison to PMMA (see Eqs. 2.9 and 2.10). However, the increased damping of these materials might counteract this dependence.

2.6 Comparison with Experiments

In this section we compare the results of our calculations with experiments reported in literature.

Firstly, we address the HWHM of the phase contrast on the surface above a buried particle. For a gold particle with a radius of 50 nm embedded 400 nm deep in PMMA, the HWHM is 4.25 μm in the FEA results and 400 nm in the analytical results. Both widths are significantly larger than the radius of the particle. In reality we expect the measured width to lie in between these two values, as the analytical results underestimate the amount of reflections and the FEA results overestimate them. The prediction of a significantly larger width stands in contrast to the observations reported in literature [3, 6, 8, 9, 11, 12], which all show a HWHM width that is comparable to the radius of the particle. Based on a width estimation of the phase contrast image of reference [6], this is even true for gold particles with a diameter of only ~ 17.5 nm embedded 500 nm deep in a polymer.

In experiments described by Shekhawat and Dravid [6], the phase contrast above an individual embedded particle seems to be independent of the distance to other particles. In contrast to this, we have seen in Sect. 2.4 that lattice effects, which are equivalent to the presence of nearby scatterers, averages out the phase contrast. However, if there is a large loss of amplitude of the

scattered waves during reflections at the top and bottom interfaces (on the basis of acoustical impedances), we expect the lattice effect to be greatly reduced.

Finally, a phase contrast of ≈ 50 mdeg is reported by Shekhawat and Dravid [6] for buried voids in interconnect copper lines. To compare this value, we used our FEA model to calculate the phase contrast of a spherical void with a radius of 50 nm buried 200 nm deep in copper. We received a phase contrast of 1 mdeg at an excitation frequency of 3 MHz. This value is $50\times$ smaller than the experimental value and could be explained by a combination of the following effects. One reason for this discrepancy might be the fully reflecting boundary conditions in our FEA model, in which we neglect the partial emission into the air above the sample or into the material underneath it. Such losses can increase contrast. Another explanation could be the excitation of planar sample resonances in the experiment, as these modes are in the order of a few MHz for realistic samples (~ 5 mm). Also one should consider that the void in the experiment was not spherical and much larger than 50 nm. In addition, on the basis of the results of Chap. 6, we expect that the contrast in these systems is caused by variations in the local effective elastic response of the sample, which is induced by the presence of the subsurface (gas) voids.

The above described discrepancies result in open questions that should be carefully addressed in future experiments to further clarify the mechanism of the contrast formation in Heterodyne Force Microscopy experiments.

2.7 Conclusion

In conclusion, we have used finite element analysis and analytical calculations to quantitatively predict both the amplitude and the phase contrast for Subsurface-AFM measurements. We found that the contrasts are generated by Rayleigh scattering at embedded particles or voids. We verified the typical Rayleigh dependencies of the amplitude and phase contrasts on the density difference between the bulk and the scattering particle, on the radius of the particle and, with some restrictions, on the frequency of the external incoming wave. The deviation of the latter dependence is due to the nontrivial frequency dependence of the Hankel functions and the effective incident field A_{eff}.

For a typical gold particle with a radius of 50 nm embedded 200 nm deep in PMMA, the expected phase contrast is 5 mdeg at an excitation frequency of 3 MHz. At the same conditions, the expected amplitude contrast is only in the order of 10^{-4}. These values for both the phase and the amplitude contrast are rather low and, therefore, very difficult to measure experimentally. We expect that it is easier to measure the phase contrast, which is probably the reason for the publication of only phase contrast images [3, 6, 8–12, 14]. As a general rule, one should try to apply as high as possible frequencies, as this will significantly increase both contrasts.

An important issue in the field of Subsurface-AFM is the determination of

the depth of a certain structure. In the case of a buried particle or void, for which Rayleigh scattering applies, we expect the contrast to vary with $1/depth$ according to our analytical calculation. However, this calculation neglects reflections of the scattered wave at sample interfaces. In contrast, the FEA results do not show a depth dependence. This is because the fully reflecting boundary conditions lead to the interference of many waves that average out the depth dependence. As one should take into account an amplitude reduction at each interface reflection according to acoustical impedances, we expect the reality to be between the analytical and the FEA calculation. As the geometry of the setup and the specific way of measuring makes it impossible to create interfaces with matched acoustical impedances, reflections will significantly influence the contrast and the FEA results should be closer to the reality. However, a depth dependence is still possible and should be, therefore, addressed experimentally.

Evaluating the lateral resolution by the phase contrast on the surface, we found that a gold particle with a radius of 50 nm buried 200 nm deep in PMMA and excited at 3 MHz appears much wider in the FEA calculations (HWHM $\sim 4.25\,\mu$m) than in the analytical calculations (HWHM $\sim$ 150 nm). Both widths are significantly larger than the particle radius, which seems to be in contradiction to reported experiments where the measured width is similar to the radius. It seems as the analytical calculations do describe the width in the phase contrast more accurately than the FEA. This would imply that reflections at the interfaces are of less importance in practice and that a depth dependence might still be possible.

All discrepancies between the analytical calculation and the FEA results are due to the different treatment of the reflections at the sample interfaces. It is important to notice that the amplitude of a reflected wave greatly depends on the acoustical impedances at this interface. The better these impedances match, the smaller will be the amplitude of the reflected wave. In addition, as damping within the bulk of the sample also reduces the amplitude of travelling sound waves, the number of reflections are reduced with high material damping. Therefore the acoustical impedances, mainly at the lower and upper interface of the sample, as well as damping in the bulk will significantly influence the contrast pattern at the surface.

To get a more detailed understanding on the contrast formation, future experiments are required that can be compared to our predictions.

Appendices of Chapter 2

2.A Calculation of the Effective Amplitude A_{eff}

We calculate the effective field A_{eff} using the scalar potential Φ [41]. We have 3 different materials: Silicon, PMMA, and air, forming a trilayer with 2

interfaces: Silicon/PMMA and PMMA/Air. Each material has its own complex wave number (damping is included): k_{Si}, k_{PMMA} and k_{Air}. At the Silicon/PMMA interface we have an incoming plane pressure wave of angular frequency ω and amplitude Φ_0. At this interface the wave is partly reflected (Φ^-_{Si}) back into the Silicon and partly transmitted into the PMMA layer (Φ^+_{PMMA}). The wave in the PMMA layer encounters the PMMA/Air interface where it also gets partly reflected (Φ^-_{PMMA}) back into the PMMA and partly transmitted into the Air (Φ^+_{Air}). The wave transmitted into the air is assumed never to come back at the interface. We can mathematically express the total potentials in the materials as follows:

$$\begin{aligned} \Phi_{Si}(z) &= \Phi_0 e^{ik_{Si}z} + \Phi^-_{Si} e^{-ik_{Si}z} && (2.12)\\ \Phi_{PMMA}(z) &= \Phi^+_{PMMA} e^{ik_{PMMA}z} \\ &\quad + \Phi^-_{PMMA} e^{-ik_{PMMA}z} && (2.13)\\ \Phi_{Air}(z) &= \Phi^+_{Air} e^{ik_{Air}z} && (2.14) \end{aligned}$$

The continuity of the normal velocity and the continuity of the normal stress at the 2 interfaces leads to 4 equations with Φ^-_{Si}, Φ^+_{PMMA}, Φ^-_{PMMA}, and Φ^+_{Air} as 4 unknowns.

$$\frac{\partial \Phi_{Si}}{\partial z}|_{z=0} = \frac{\partial \Phi_{PMMA}}{\partial z}|_{z=0} \quad (2.15)$$

$$\frac{\partial \Phi_{PMMA}}{\partial z}|_{z=0} = \frac{\partial \Phi_{Air}}{\partial z}|_{z=0} \quad (2.16)$$

$$(K_{Si} + 4G_{Si}/3)\frac{\partial^2 \Phi_{Si}}{\partial^2 z}|_{z=t} = (K_{PMMA} + 4G_{PMMA}/3)\frac{\partial^2 \Phi_{PMMA}}{\partial^2 z}|_{z=t} \quad (2.17)$$

$$(K_{PMMA} + 4G_{PMMA}/3)\frac{\partial^2 \Phi_{PMMA}}{\partial^2 z}|_{z=t} = (K_{Air} + 4G_{Air}/3)\frac{\partial^2 \Phi_{Air}}{\partial^2 z}|_{z=t} \quad (2.18)$$

, where K denotes the bulk modulus and G the shear modulus. We can determine Φ^-_{Si}, Φ^+_{PMMA}, Φ^-_{PMMA}, and Φ^+_{Air} in terms of of Φ_0 and the thickness t of the PMMA layer.

The effective amplitude incoming at the scatterer at position $(t-d)$ is given by $\partial \Phi_{PMMA}/\partial z|_{z=t-d}$. This calculated amplitude is used as the effective incident amplitude A_{eff} at the scatterer, from which we determine the scattering amplitude. The effective amplitude at the surface is given by $\partial \Phi_{PMMA}/\partial z|_{z=t}$.

2.B Expansion of C_A and C_ϕ

We start with Eqs. 2.2 and 2.3. Keeping in mind that the amplitude at the surface is given by $\mathrm{A_{eff}} + \mathrm{A_s}$ and that $\mathrm{A_s}$ is much smaller than $\mathrm{A_{eff}}$, we expand C_A and C_ϕ as follows.

$$|A| \cdot C_\mathrm{A} = |A + A_\mathrm{s}| - |A| \tag{2.19}$$

$$\approx |A| \left(1 + \frac{Re[A^* A_\mathrm{s}]}{|A|^2} + \frac{|A_\mathrm{s}|^2}{2|A|^2}\right) - |A| \tag{2.20}$$

$$\approx |A| \frac{Re[A^* A_\mathrm{s}]}{|A|^2} \tag{2.21}$$

We used the Taylor expansion of $\sqrt{1+x}$ around $x = 0$ and we have neglected $|A_s|^2$, because it scales with $f^4 R^6$. This leads to

$$C_A = \frac{Re[A^* A_\mathrm{s}]}{|A|^2} \tag{2.22}$$

Before expanding C_ϕ, we first introduce $\phi_0 = tan^{-1}(Im[A]/Re[A])$. The expansion of C_ϕ is:

$$C_\phi = \tan^{-1}\left(\frac{Im[A + A_\mathrm{s}]}{Re[A + A_\mathrm{s}]}\right) - \phi_0 \tag{2.23}$$

$$\approx \tan^{-1}\left(\frac{Im[A]}{Re[A]}(1 + \frac{Im[A_\mathrm{s}]}{Im[A]})(1 - \frac{Re[A_\mathrm{s}]}{Re[A]})\right) - \phi_0 \tag{2.24}$$

$$\approx \tan^{-1}\left(\frac{Im[A]}{Re[A]}(1 + \frac{Im[A_\mathrm{s}]}{Im[A]} - \frac{Re[A_\mathrm{s}]}{Re[A]})\right) - \phi_0 \tag{2.25}$$

$$\approx \frac{Re[A]Im[A]}{|A|^2}\left(\frac{Im[A_\mathrm{s}]}{Im[A]} - \frac{Re[A_\mathrm{s}]}{Re[A]}\right) \tag{2.26}$$

$$= \frac{Im[A^* A_\mathrm{s}]}{|A|^2} \tag{2.27}$$

We neglected $Re[A_s]Im[A_s]$ and used the following Taylor expansions:

$$\frac{1}{1-x} \approx 1 + x \tag{2.28}$$

$$\arctan\left(\tan(a) \cdot (1 + x)\right) \approx a + \frac{\tan(a)}{1 + \tan^2(a)} x \tag{2.29}$$

2.C Depth Dependence of C_A and C_ϕ in FEA

In this appendix, we calculate the expected depth dependence for the FEA calculations. We treat two different contributions: the amplitude A_{eff} on the

surface, and the amplitude A_s of the scattered wave. We take into account the damping length L_α of the sample, the thickness t of the sample, the depth d of the subsurface scatterer, and the 180 degrees phase shift when the sound wave reflects at the bottom interface.

Let us first discuss the amplitude of the excitation wave. The amplitude of the ultrasonic sample excitation is A_{ext}. Before the wave reaches the surface of the sample, it lost an amplitude equal to σA_{ext} according to standard Rayleigh scattering by the subsurface scatterer. In the end, we have to take into account all possible reflections between the top and bottom interface, which results in the following, simplified, expression for the amplitude A_{eff} on the surface above the nanoparticle:

$$\begin{aligned} A_{eff} &= \sum_{n=1}^{\infty} \left[-(1-\sigma)e^{-2t/L_\alpha}\right]^n A_{ext} e^{-t/L_\alpha} \\ &= e^{-t/L_\alpha} \left[\frac{(1-\sigma)e^{-2t/L_\alpha}}{1+(1-\sigma)e^{-2t/L_\alpha}}\right] A_{ext} \end{aligned} \tag{2.30}$$

Equation 2.30 shows that the amplitude A_{eff} on the surface does not depend on the depth of the subsurface scatterer. The calculation for the amplitude A_s of the scattered wave has two contributions: one contribution comes from the scattered wave in the $+\vec{r_0}$ direction, and the other one from the scattered wave in the $-\vec{r_0}$ direction (see Fig. 2.1). A similar calculation as in Eq. 2.30 gives us the following expression for A_s:

$$\frac{A_s}{A_{ext}} = \sigma \frac{A_{eff}}{A_{ext}} \left[\frac{R}{\sqrt{4\pi}d} - \frac{R}{\sqrt{4\pi}(d+2t)}\right] \tag{2.31}$$

, in which R is the radius of the nanoparticle and a typical distance over which the depth dependence of the scattered wave diminishes. We observe in Eq. 2.31 that the amplitude A_s of the scattered wave at the surface does depend on the depth of the subsurface scatterer. Using the expressions for the amplitude A_{eff} and the scattered amplitude A_s in Eqs. 2.2 and 2.3, we find that the total difference in amplitude, due to the presence of the nanoparticle, is given by:

$$A_{tot} = \left(\frac{x\sqrt{x}}{1+x}\right)\sigma \left[\left(\frac{x}{1+x}\right) - 1 + \left(\frac{R}{\sqrt{4\pi}d} - \frac{R}{\sqrt{4\pi}(d+2t)}\right)\right] A_{ext} \tag{2.32}$$

, in which we used that $\sigma << 0$ and we introduced $x = \exp(-2t/L_\alpha)$. As $|x| \approx 1$ and $d_0 < d$ in the FEA calculations, only the depth independent part of Eq. 2.32 is left and we do not see a depth dependence.